

Vibronic coupling in a molecular 4f qubit

Jonathan Marbey^{a,b,†}, Jon G. C. Kragoskow^{c,†}, Christian D. Buch,^d Joscha Nehrkorn^a, Mykhaylo Ozerov^a, Stergios Piligkos^{d,*}, Stephen Hill^{a,b,*} and Nicholas F. Chilton^{c,*}

^a National High Magnetic Field Laboratory, Tallahassee, Florida, 32310, United States of America

^b Department of Physics, Florida State University, Tallahassee, Florida, 32306, United States of America

^c Department of Chemistry, School of Natural Sciences, University of Manchester, Oxford Road, Manchester, M13 9PL, United Kingdom

^d Department of Chemistry, University of Copenhagen, DK-2100 Copenhagen, Denmark

[†] These two authors contributed equally to this work.

Email: piligkos@chem.ku.dk; shill@magnet.fsu.edu; nicholas.chilton@manchester.ac.uk

Vibronic coupling, the interaction between molecular vibrations and electronic states, is a pervasive effect that profoundly affects chemical processes. In the case of molecular magnetic materials, vibronic, or spin-phonon, coupling leads to magnetic relaxation, which equates to loss of magnetic memory and loss of phase coherence in molecular magnets and qubits, respectively. The study of vibronic coupling is challenging, and most experimental evidence is indirect. Here we employ far-infrared magnetospectroscopy to probe vibronic transitions in a Yb^{III} molecular qubit directly. We find intense signals near electronic states, which we show arise due to an “envelope effect” in the vibronic coupling Hamiltonian, and we calculate the vibronic coupling fully *ab initio* to simulate the spectra. We subsequently show that vibronic coupling is strongest for vibrational modes that simultaneously distort the first coordination sphere and break the C₃ symmetry of the molecule. With this knowledge, vibrational modes could be identified and engineered to shift their energy towards or away from particular electronic states to alter their impact. Hence, these findings provide new insights towards developing general guidelines for the control of vibronic coupling in molecules.

Vibronic coupling is pervasive – all materials vibrate and have electronic states – and its impact is crucial in many settings. For example, it is thought to be central in photosynthesis^{1,2} and in light-harvesting proteins,³ but, more generally, it is implicated in enantioselective catalysis⁴ and luminescent materials,⁵ and is pivotal in the operation of molecular qubits^{6,7} and single-molecule magnets.⁸ Synthetic chemists have made extensive strides in controlling vibronic coupling through judicious molecular design,⁹ but the community at large is far from general design guidelines to control such effects. A key roadblock to progress is obtaining direct evidence of vibronic coupling: conventional experiments probing magnetic relaxation and quantum phase coherence only probe the effects of vibronic coupling indirectly,^{6–8,10} and studies using direct probes such as ultrafast^{9,11} or

infrared (IR)^{12–14} spectroscopies are rare. To this end, here we perform far-IR magnetospectroscopy (FIRMS)^{15,16} measurements on the Yb^{III} qubit [Yb(trensal)] (**1**, where H₃trensal = 2,2,2-tris(salicylideneimino)trimethylamine, Figure 1, chosen due to its extensive existing magnetic and spectroscopic characterisation^{10,17–21}) to directly probe the vibronic coupling in this molecule, and develop *ab initio* simulations of the FIRMS map to elucidate the origins of the vibronic transitions. A FIRMS map is obtained from a series of far-IR spectra collected in varying magnetic fields, which is then normalised to remove field-independent signals corresponding to purely vibrational modes. Thus, a FIRMS map highlights vibronic transitions which involve a simultaneous change in both electronic and vibrational states due to absorption of an IR photon; this is distinct from transitions between electronic states induced by absorption of phonons, which are the origin of magnetic relaxation in single-molecule magnets and quantum decoherence in molecular qubits. Nonetheless, we can learn a great deal about these latter effects from measurement and simulation of the vibronic coupling.

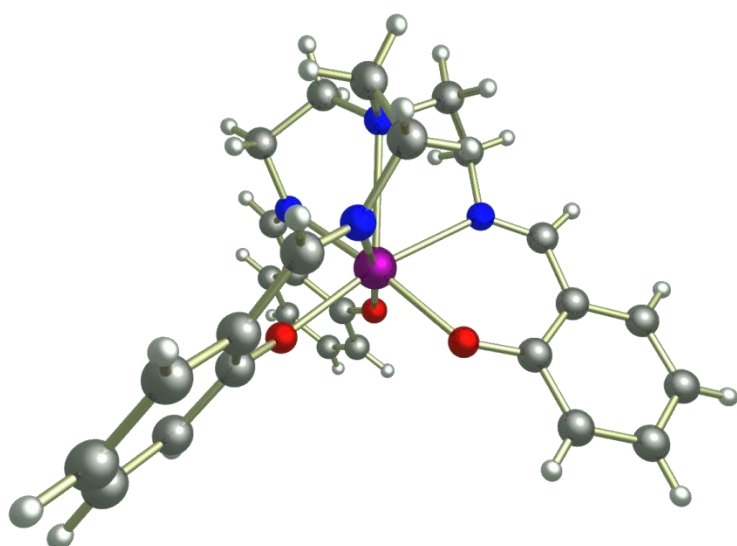


Figure 1. Structure of [Yb(trensal)] (1**) viewed perpendicular to the C₃ axis.** Hydrogen = white, carbon = grey, nitrogen = blue, oxygen = red, ytterbium = purple.

Complex **1** has C₃ point symmetry and crystallises in the P $\bar{3}$ c1 space group. Yb^{III} has a 4f¹³ ground configuration which is split into the ground ²F_{7/2} and excited ²F_{5/2} multiplets by spin-orbit coupling (Figure 2, inset), which are then further split by the crystal field (CF) of the molecule; in the absence of a magnetic field all states are doubly degenerate owing to Kramers theorem.²² Some of us have previously reported near-IR absorption and luminescence measurements of **1** in a diamagnetic host [Yb_{0.07}Lu_{0.93}(trensal)] (**1'**) and have experimentally determined the CF splitting of both spin-orbit multiplets. Fitting the magnetic susceptibility, magnetisation, and optical data simultaneously with a CF Hamiltonian (Tables S1 and S2), yields effective *g*-values for the ground doublet which match those from electron paramagnetic resonance (EPR) spectroscopy.²⁰ This reveals considerable axial

and trigonal contributions to the CF, where nearly all states are mixtures of m_j functions, except for the 3rd Kramers doublet (KD) which comprises the pure $m_j = \pm 3/2$ states as these cannot mix with other m_j states in C_3 symmetry. Additional peaks are found in the luminescence spectrum of **1'** which do not correspond to CF energy levels of the $^2F_{7/2}$ multiplet (Figure 2, e.g., peaks 2a and 2b); these were attributed to “vibrational side-bands” in the original paper,¹⁰ but the true nature of these features was unknown. Herein we collect and perform a detailed theoretical analysis of the FIRMS map of **1** to study the vibronic coupling. We find that vibronic transitions appear near CF states due to a hitherto undescribed “envelope effect”, and that vibronic coupling is strongest for vibrational modes that distort the first coordination sphere of Yb^{III} as well as breaking the C_3 point symmetry. Such findings are paramount in unravelling the complex nature of vibronic coupling and for developing future molecular design criteria to deliver control of this phenomenon.

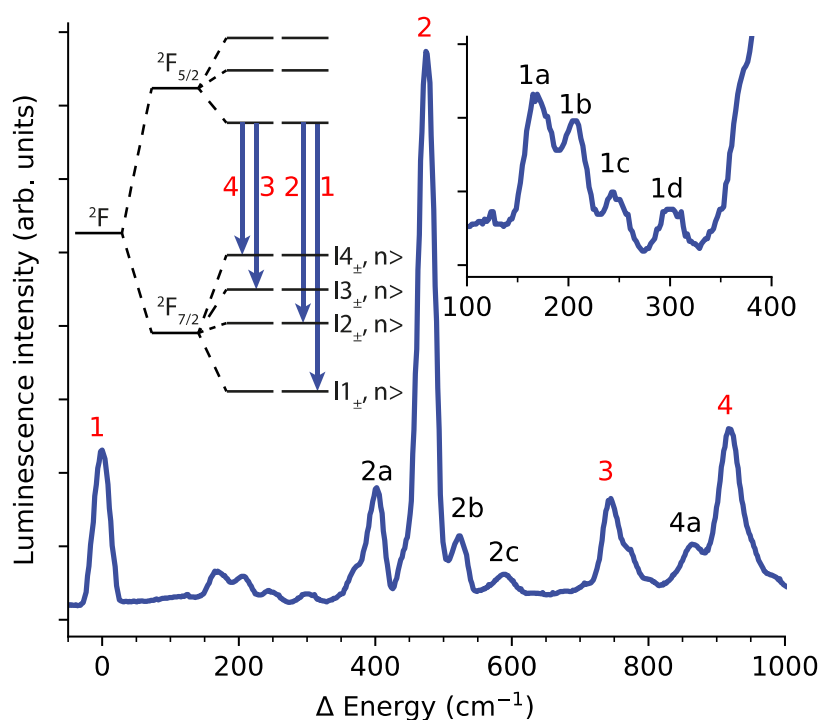


Figure 2. Measurement and assignment of low-lying electronic states in [Yb(trensal)]. Experimental luminescence (emission) spectrum of [Yb_{0.07}Lu_{0.93}(trensal)] (**1'**) at 5 K.¹⁰ Transitions are from the lowest KD of the excited $^2F_{5/2}$ spin-orbit multiplet to the different KDs of the ground $^2F_{7/2}$ multiplet (inset left; not to scale) and occur in the near-IR around 980 nm.^{10,23} The spectrum is plotted as energy differences with respect to the zero-phonon line of the ground KD (peak 1), thus the spectrum is reversed compared to a conventional emission spectrum. The energies of the four KDs of the $^2F_{7/2}$ multiplet, as determined from the spectrum relative to the ground KD at 0 cm⁻¹ (1) are: 474 cm⁻¹ (2), 745 cm⁻¹ (3) and 920 cm⁻¹ (4). Additional features are at 169 cm⁻¹ (1a), 207 cm⁻¹ (1b), 247 cm⁻¹ (1c), 302 cm⁻¹ (1d), 403 cm⁻¹ (2a) and 524 cm⁻¹ (2b), 588 cm⁻¹ (2c), 864 cm⁻¹ (4a).

Results and Discussion

Ab initio electronic structure

Using the structure from X-ray diffraction (XRD), complete active space self-consistent field calculations with extended multi-state perturbative corrections and spin-orbit coupling (CASSCF-XMS-CASPT2-SO; see Methods) are in excellent agreement with the experimentally-determined CF energies, however the first excited state appears $\sim 60\text{ cm}^{-1}$ lower than experiment (Figure S1, Tables S2 and S3). The composition of the ground KD is very similar to the experimental CF model and to EPR data ($g_{\parallel,\text{calc}} = 4.68$ and $g_{\perp,\text{calc}} = 2.80$, *cf.*, $g_{\parallel,\text{exp}} = 4.29$ and $g_{\perp,\text{exp}} = 2.90$).²⁰ Optimisation of the structure of **1** using density-functional theory (DFT, see Methods) yields the structure **1_{opt}** (Table S4), which shows only minor structural changes (root mean squared deviation of 0.127 \AA compared to **1**). The vibrational modes of **1_{opt}** are classified as A (singly degenerate) or E (doubly degenerate) irreducible representations of the C_3 point group (Table S5), and we find good agreement between the calculated vibrational energies and the experimental Fourier transform IR (FTIR) spectrum in zero-field (Figure S2). CASSCF-XMS-CASPT2-SO calculations on **1_{opt}** give a slightly worse agreement with the experimental electronic energy spectrum overall (Figure S1), though the first excited state is now only $\sim 30\text{ cm}^{-1}$ higher than the experimental value and the ground state g -values remain practically unchanged (Table S6). The considerable impact of small structural changes on the electronic states of **1** (first excited state shifts by $\sim 100\text{ cm}^{-1}$) indicates that the electronic structure of **1** is highly susceptible to molecular distortion, providing a physical basis for significant vibronic coupling found for this molecule.

FIRMS map and model Hamiltonian

A FIRMS map highlights vibronic transitions driven by IR photons with energy $h\nu$. The positions of vibronic transitions are $h\nu = \Delta_e \pm \Delta_v$, where Δ_e is the difference in electronic energy and Δ_v is the difference in vibrational energy. The intensity of a vibronic transition in a FIRMS map is related to both the intensities of IR absorption of the pure vibrational and the pure electronic transitions, but also the strength of vibronic coupling between the vibration and the electronic states involved. The FIRMS map for **1** (Figure 3) reproduces the vibronic side-bands observed in luminescence measurements (Figure 2), and reveals evidence of their movement (along with several other features) as a function of applied magnetic field. While the zero-field FTIR spectrum of **1** shows vibrational modes ranging from 0 to 900 cm^{-1} , in good agreement with our DFT calculations (Figure S2), the FIRMS map shows far fewer field-dependent signals that appear in bands from 370 - 550 cm^{-1} and 740 - 815 cm^{-1} (Figures 3a and S5b) near the energies of the electronic doublets in **1** (474 and 745 cm^{-1}). Interestingly, the spectrum shows field-dependent vibronic signals below the energy of the first excited doublet (*i.e.*, 370 - 474 cm^{-1}), which mainly arise from very low-energy intra-KD electronic transitions coupled to vibrational excitations near the observed transition energy (hot

transitions are very unlikely at 4.2 K, see below and Figure S3). Given this, it is odd that vibronic transitions are not observed in other ranges with significant IR absorption, for instance around 200 cm^{-1} . We first develop a simple toy model to gain qualitative fundamental understanding of this pattern before moving onto a full *ab initio* analysis of the spectrum.

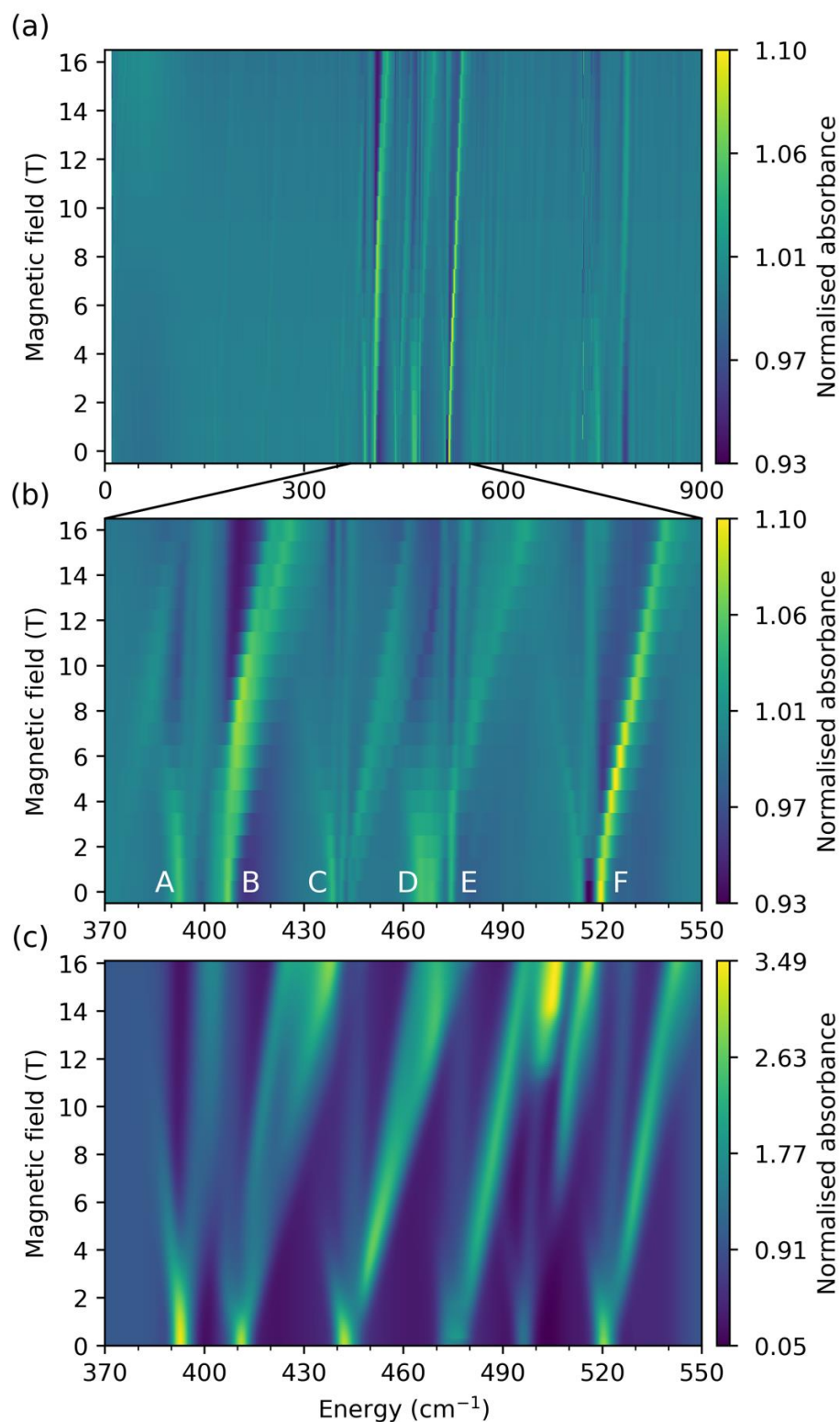


Figure 3. Experimental and simulated FIRMS maps for 1. Experimental FIRMS map measured at 4.2 K in the range (a) 0-900 cm^{-1} and (b) 370-550 cm^{-1} (field dependent signals are labelled as **A-F**). (c) Composite *ab initio* simulated FIRMS map for signals **A-F** using XMS-CASPT2-SO equilibrium CF parameters with experimental CF energies and CASSCF-SO vibronic couplings (see Methods and Supporting Information); this composite image was generated from two independent simulations including vibrational modes 34-42 and 4-5 (Table S5). The colour bars show fractional changes in relative transmittance (normalised absorbance) due to the magnetic field.

FIRMS maps have been expertly modelled by Atanasov and Neese,²⁴ among others,¹²⁻¹⁴ and we follow a similar conceptual approach. Our simple toy model consists of two electronic KDs separated by Δ , coupled to a single vibrational mode of energy $\hbar\omega$, for which we consider only the ground $n = 0$ and first excited $n = 1$ vibrational quantum states. We label the states as $|N_{\pm}, n\rangle$ where N is the index of the electronic state, \pm represents each state of the KD, and n is the vibrational state. For simplicity, we assume both KDs have the same g -values and hence parameterize the effect of the magnetic field as $\delta = g\mu_B B/2$ (Figure 4). Without vibronic coupling, the zeroth-order Hamiltonian \hat{H}_0 of this toy model in the direct product basis $\{|1_{-}, 0\rangle, |1_{-}, 1\rangle, |1_{+}, 0\rangle, |1_{+}, 1\rangle, |2_{-}, 0\rangle, |2_{-}, 1\rangle, |2_{+}, 0\rangle, |2_{+}, 1\rangle\}$ is:

$$\hat{H}_0 = \begin{bmatrix} -\delta & 0 & 0 & 0 & 0 & 0 & 0 & 0 \\ 0 & -\delta + \hbar\omega & 0 & 0 & 0 & 0 & 0 & 0 \\ 0 & 0 & \delta & 0 & 0 & 0 & 0 & 0 \\ 0 & 0 & 0 & \delta + \hbar\omega & 0 & 0 & 0 & 0 \\ 0 & 0 & 0 & 0 & \Delta - \delta & 0 & 0 & 0 \\ 0 & 0 & 0 & 0 & 0 & \Delta - \delta + \hbar\omega & 0 & 0 \\ 0 & 0 & 0 & 0 & 0 & 0 & \Delta + \delta & 0 \\ 0 & 0 & 0 & 0 & 0 & 0 & 0 & \Delta + \delta + \hbar\omega \end{bmatrix} \quad 1$$

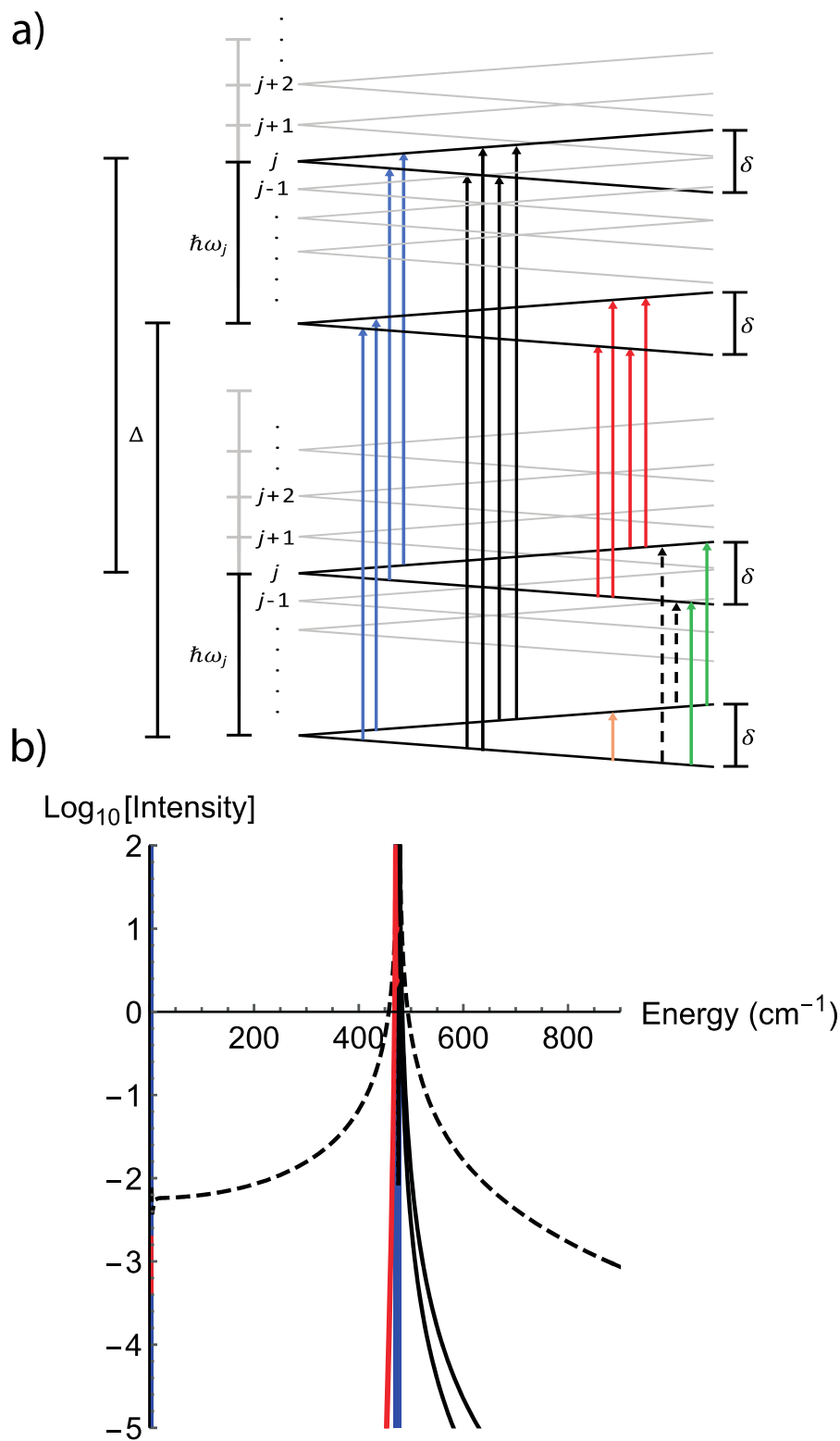


Figure 4. Vibronic states and theoretical FIRMS intensity for toy model. (a) States of toy model; note that the vibrational energy $\hbar\omega_j$ is a variable, and all values are considered in (b). Purely electronic transitions are shown in blue, purely vibrational transitions in green, cold vibronic inter-KD transitions in black, hot vibronic transitions in red, and cold vibronic intra-KD transitions in dashed black; EPR transitions (not studied in this work) in orange. (b) Absorption intensity for cold intra-KD vibronic transitions (black dashed lines), cold inter-KD vibronic transitions (solid black lines), hot

inter-KD vibronic transitions (red solid lines), and purely electronic (solid blue lines) transitions, under irradiation from an IR source with uniform intensity and uniform vibronic coupling. Purely vibrational transitions are not shown. Constructed with model parameters $F = G = 0.1 \text{ cm}^{-1}$, $A_v = 1$, $A_e = 10^2$, $\Delta = 474 \text{ cm}^{-1}$ and $\delta = 2 \text{ cm}^{-1}$ (field ca. 2 T, see Equations 3 and 4).

Vibronic transitions involve a change in both the electronic and vibrational states, otherwise they are purely electronic or purely vibrational. There are two types of vibronic transitions in this toy model: intra-KD transitions (dashed black arrows in Figure 4a) and inter-KD transitions (solid black and red arrows in Figure 4a). Due to the low temperature of the experiment (4.2 K) and large CF splitting ($\Delta = 474 \text{ cm}^{-1}$), all absorptions must arise from the four initial states $|1_-, 0\rangle$, $|1_-, 1\rangle$, $|1_+, 0\rangle$ or $|1_+, 1\rangle$, and for magnetic fields $> 5 \text{ T}$ and vibrational modes with $\hbar\omega > 20 \text{ cm}^{-1}$, only cold transitions originating from $|1_-, 0\rangle$ are relevant (Figure S3). We define the transition matrix elements due to the IR radiation between electronic states as A_e and between vibrational states as A_v (Equation S1). For the system without vibronic coupling described by \hat{H}_0 , the only possible transitions are purely electronic at $h\nu = 2\delta$, $h\nu = \Delta$ and $h\nu = \Delta \pm 2\delta$ (intensities proportional to A_e^2) or purely vibrational at $h\nu = \hbar\omega$ (intensities proportional to A_v^2); the observation of multiple transitions in the vicinity of a single electronic excitation in the FIRMS map provides direct evidence for the vibronic coupling. Anticipating our *ab initio* model (see Supporting Information), we define the vibronic coupling as perturbations to the electronic states in the weak-coupling limit: diagonal terms G express energy shifts and off-diagonal terms F describe coupling between different electronic states (Equation S2). The coupling Hamiltonian \hat{H}_1 in the direct product basis is (block structure highlighted for clarity):

$$\hat{H}_1 = \begin{bmatrix} 0 & G & 0 & F & 0 & F & 0 & F \\ G & 0 & F & 0 & F & 0 & F & 0 \\ 0 & F & 0 & G & 0 & F & 0 & F \\ F & 0 & G & 0 & F & 0 & F & 0 \\ 0 & F & 0 & F & 0 & G & 0 & F \\ F & 0 & F & 0 & G & 0 & F & 0 \\ 0 & F & 0 & F & 0 & F & 0 & G \\ F & 0 & F & 0 & F & 0 & G & 0 \end{bmatrix} \quad 2$$

We can determine the eigenstates of $\hat{H}_0 + \hat{H}_1$ with first-order perturbation theory (Equation S3) and hence calculate the intensity of FIRMS transitions. Considering the cold intra-KD vibronic transition (absorption of an IR photon with $h\nu = 2\delta + \hbar\omega$), under the approximation that $\delta \ll \Delta$ and $\delta \ll \hbar\omega$ we obtain:

$$I(|1_-, 0\rangle \rightarrow |1_+, 1\rangle) \propto \left(\frac{2F(A_v F \hbar^2 \omega^2 - 2A_e \Delta \hbar^2 \omega^2 + A_v G (\hbar^2 \omega^2 - \Delta^2))}{\hbar^2 \omega^2 (\hbar^2 \omega^2 - \Delta^2)} \right)^2 \quad 3$$

The intensity of this transition thus increases when the vibronic coupling (F and G), the electronic transition intensity (A_e) or the vibrational transition intensity (A_v) increase. But notably, the intensity diverges (in first-order perturbation theory, due to coupling between $|1_+, 1\rangle$ and $|2_+, 0\rangle$) when $\hbar\omega = \Delta$ and, therefore, this toy model predicts that we should expect intense intra-KD vibronic signals

when the energy of the vibrational mode is similar to CF gaps in the molecule: because $\delta \ll \hbar\omega$ for such intra-KD transitions, these appear in the regime where $h\nu \approx \hbar\omega \approx \Delta$ (Figure 4b; *n.b.*, this transition does not involve absorption of a phonon at $\hbar\omega$ to generate an electronic excitation at Δ). This is a general conclusion that applies to other FIRMS experiments; indeed, such effects have been observed previously but not explained.¹² Similar expressions occur for the inter-KD vibronic transitions (Equations S4 and S5, under the approximation that $\hbar\omega \ll \Delta$ and $\delta \ll \Delta$), that diverge when $\delta \rightarrow 0$ and/or $\hbar\omega \rightarrow 0$ (*i.e.* in proximity to purely electronic transitions). From these results we are able to calculate a theoretical FIRMS intensity spectrum for each class of transition (Figure 4b). As expected from Equations 3, S4 and S5, our theoretical spectrum predicts envelopes of increased intensity for vibronic transitions around $h\nu = \Delta$, in agreement with experiment; we expect enhanced vibronic intensity near the second excited KD at 745 cm⁻¹ for the same reasons (not included in this toy model). Thus, our toy model explains the “envelope effect” of the FIRMS map with intensity concentrated in the regions 370-550 cm⁻¹ and 740-815 cm⁻¹.

Ab initio FIRMS analysis

Moving beyond simple toy models where state energies and vibronic coupling are parameters, we now endeavour to understand the details of the FIRMS map of **1** (Figure 3) by calculating the vibronic coupling *ab initio*. The conceptual framework is similar to the toy model, but now we consider the realistic details of **1**, where the energies of the coupled electronic and vibrational states as a function of magnetic field are obtained from the total Hamiltonian \hat{H}_T :

$$\begin{aligned}\hat{H}_T &= \hat{H}_{CF} + \hat{H}_{Zee} + \sum_j [\hat{H}_{vib,j} + \hat{H}_{coup,j}] \\ &= \sum_{k=2,4,6} \sum_{q=-k}^k B_k^q \hat{O}_k^q + \mu_B g_J \vec{B} \cdot \vec{J} + \sum_{j=1}^{3N-6} \left[\hbar\omega_j \left(n_j + \frac{1}{2} \right) + \hat{H}_{coup,j} \right]\end{aligned}\quad 4$$

The first and second terms are the electronic CF and Zeeman Hamiltonians, evaluated in the $|m_j\rangle$ basis of the ground $^2F_{7/2}$ spin-orbit multiplet of Yb^{III}, the third term is the quantum harmonic oscillator Hamiltonian, evaluated in the basis of vibrational quanta $|n_j\rangle$ for mode j , and the fourth term $\hat{H}_{coup,j}$ is the vibronic coupling Hamiltonian; μ_B is the Bohr magneton, g_J is the Landé g -factor for Yb^{III}, \vec{B} is the magnetic field vector, \vec{J} is the electronic total angular momentum vector operator, B_k^q are the Stevens CF parameters (CFPs), \hat{O}_k^q are the Stevens operators, $\hbar\omega_j$ is the energy of vibrational mode j , \hbar is the reduced Planck constant, and N is the number of atoms. As $\hat{H}_{CF} + \hat{H}_{Zee}$ commutes with each $\hat{H}_{vib,j}$, and all $\hat{H}_{vib,j}$ commute with one-another in the harmonic approximation, Equation 4 can be written in the direct product basis $|m_j, n_1, n_2, \dots\rangle$ (see Supporting information). \hat{H}_{CF} is constructed using CFPs from CASSCF-XMS-CASPT2-SO calculations (see Methods; this encodes all

information on the CF energies and anisotropic g -values, but we correct the former to match experiment) and each $\hbar\omega_j$ is obtained from DFT calculations (see Methods), where we only consider the $n_j = 0$ and $n_j = 1$ states (thus ignoring vibrational overtones). To construct each $\hat{H}_{\text{coup},j}$, we expand the CFPs for **1** in a Taylor series in the displacement Q_j along normal mode j around equilibrium $Q_{\text{eq}} = 0$:²⁵

$$B_k^q(Q_j) = B_k^q(Q_{\text{eq}}) + \sum_j^{3N-6} Q_j \left(\frac{\partial B_k^q}{\partial Q_j} \right)_{\text{eq}} + \frac{1}{2} \sum_j^{3N-6} \sum_{j'}^{3N-6} Q_j Q_{j'} \left(\frac{\partial^2 B_k^q}{\partial Q_j \partial Q_{j'}} \right)_{\text{eq}} + \dots \quad 5$$

Here, we simulate FIRMS maps by employing a first-order approximation in which the linear term is assumed to be dominant (verified by our *ab initio* calculations, Figure S4). This assumption leads to the vibronic coupling Hamiltonian, Equation 6. We calculate the vibronic coupling coefficients $\left(\frac{\partial B_k^q}{\partial Q_j} \right)_{\text{eq}}$ with CASSCF-SO methods, and the matrix representation of Equation 6 is constructed in the direct product basis (see Supporting Information).

$$\hat{H}_{\text{coup},j} = \sum_{k=2,4,6} \sum_{q=-k}^k \hat{Q}_j \left(\frac{\partial B_k^q}{\partial Q_j} \right)_{\text{eq}} \hat{O}_k^q \quad 6$$

At equilibrium geometry, the C_3 point symmetry of **1** means that only B_k^q with $q = 0, \pm 3, \pm 6$ are non-zero. However, this constraint can be lost when the molecule vibrates and, thus, up to 27 non-zero $\left(\frac{\partial B_k^q}{\partial Q_j} \right)_{\text{eq}}$ contributions to $\hat{H}_{\text{coup},j}$ are possible. Hence, we can also define the overall vibronic coupling strength for each mode as S_j (Equation 7);²⁶ note here that $\mathcal{B}_{k,q}$ are CFPs in Wybourne notation and are linear combinations of the CFPs in Stevens notation B_k^q .²⁷

$$S_j = \sqrt{\frac{1}{3} \sum_k \frac{1}{2k+1} \sum_{q=-k}^k \left| \left(\frac{\partial \mathcal{B}_{k,q}}{\partial Q_j} \right)_{\text{eq}} \right|^2} \quad 7$$

Using this *ab initio* method of vibronic coupling, along with a simple method for calculating transition intensities and spherical integration of the magnetic field to reproduce the powder spectrum (see Supporting Information), we can simulate a FIRMS map for the electronic states of **1** coupled to selections of vibrational modes; calculation of the full vibronic manifold with all vibrational modes is far beyond current computational feasibility, and is not necessary as only modes in energetic proximity of one another need be modelled simultaneously. When considering more than one vibrational mode, $\hat{H}_{\text{coup},j}$ does not couple them directly (*i.e.*, the $\left(\frac{\partial^2 B_k^q}{\partial Q_j \partial Q_{j'}} \right)_{\text{eq}}$ term of Equation 5 is not included in Equation 6), but Equation 4 does allow vibrational mode interactions *via* the electronic states.

We focus on the most intense signals near the first electronic transition ($370\text{-}550\text{ cm}^{-1}$, Figure 3), but there is also a strong signal in proximity to the second electronic transition (775 cm^{-1}) and far weaker signals at 167 cm^{-1} , 238 cm^{-1} , 553 cm^{-1} and 581 cm^{-1} , all of which are more distant from any electronic transitions; these are discussed in the Supporting Information, along with a full assignment of the proceeding signals. Examining the $370\text{-}550\text{ cm}^{-1}$ region, we can identify intense field-dependent signals emerging from 393 , 407 , 444 , 468 , 474 , and 520 cm^{-1} in zero-field (**A-F**, respectively, Figures 3b and 5). Signals below the first CF state (*i.e.* $370\text{-}474\text{ cm}^{-1}$, **A-C**) must mainly be due to cold intra-KD vibronic transitions ($|1_{\pm}, 0\rangle \rightarrow |1_{\mp}, 1\rangle$, Figure 4, because hot transitions are very unlikely at 4.2 K , Figure S3), where the observed energy in the FIRMS map is close to the vibrational energy (as $\delta \ll \hbar\omega$ and hence $h\nu = \hbar\omega \pm 2\delta \approx \hbar\omega$). Signals above the electronic excitation (*i.e.* $474\text{-}550\text{ cm}^{-1}$, **D-F**) can either be intra- or inter-KD vibronic transitions ($|1_{\pm}, 0\rangle \rightarrow |1_{\mp}, 1\rangle$, $|1_{\pm}, n\rangle \rightarrow |2_{\pm}, n'\rangle$ or $|1_{\pm}, n\rangle \rightarrow |2_{\mp}, n'\rangle$) or purely electronic transitions ($|1_{\pm}, n\rangle \rightarrow |2_{\pm}, n\rangle$, Figure 4). Signals that move to higher energies with increasing field are electronically cold (originating from $|1_{-}, n\rangle$), whilst those moving to lower energies are electronically hot (originating from $|1_{+}, n\rangle$). On this basis, and considering the DFT-calculated vibrational spectrum, we can assign signals **A** and **B** (corresponding to peak 2a in the luminescence spectrum, Figure 2) as intra-KD transitions coupled to vibrational modes $j = 34\text{-}36$ (Figure S6, Videos S13-15), and signal **C** as an intra-KD band coupled to modes $j = 37\text{-}39$ (Figure S7, Videos S16-18). Signals **D** and **E** are complicated as they contain contributions from purely electronic and intra-KD bands coupled to modes $40\text{-}42$ (Figure S8, Videos S19-21); we rule out inter-KD hot bands (requiring $\hbar\omega < 20\text{ cm}^{-1}$) arising from acoustic phonon modes as the vibrational transition intensities will be negligible compared to intramolecular modes. Due to our approximate *ab initio* vibronic couplings, signals **D** and **E** are shifted higher in energy in our simulations versus experiment (see Supporting Information). The intense signal **F** (corresponding to peak 2b in the luminescence spectrum, Figure 2) could either be an intra-KD or an inter-KD vibronic transition, or both; the former would involve either mode 43, and/or modes 44 and 45 (Figure S9, Videos S22-S24) and the latter would involve modes 4 and 5 (Figure S10, Videos S1 and S2). Comparison of our simulations to the experiment suggest that signal **F** is an inter-KD transition coupled to modes 4 and 5, as the alternative, an intra-KD transition coupled to modes 43, 44 and 45, yields additional peaks unobserved in experiment and has the wrong intensity pattern. Hence, we can simulate the FIRMS map of **1** in the $370\text{-}550\text{ cm}^{-1}$ range by building a composite (summative) image of our *ab initio* simulations of the maps arising from coupling to vibrational modes $34\text{-}42$ (signals **A-E**) and to modes 4 and 5 (signal **F**; Figure 3c), which shows excellent agreement with the experiment; thus, we are confident in the vibronic assignments (Figure 5).

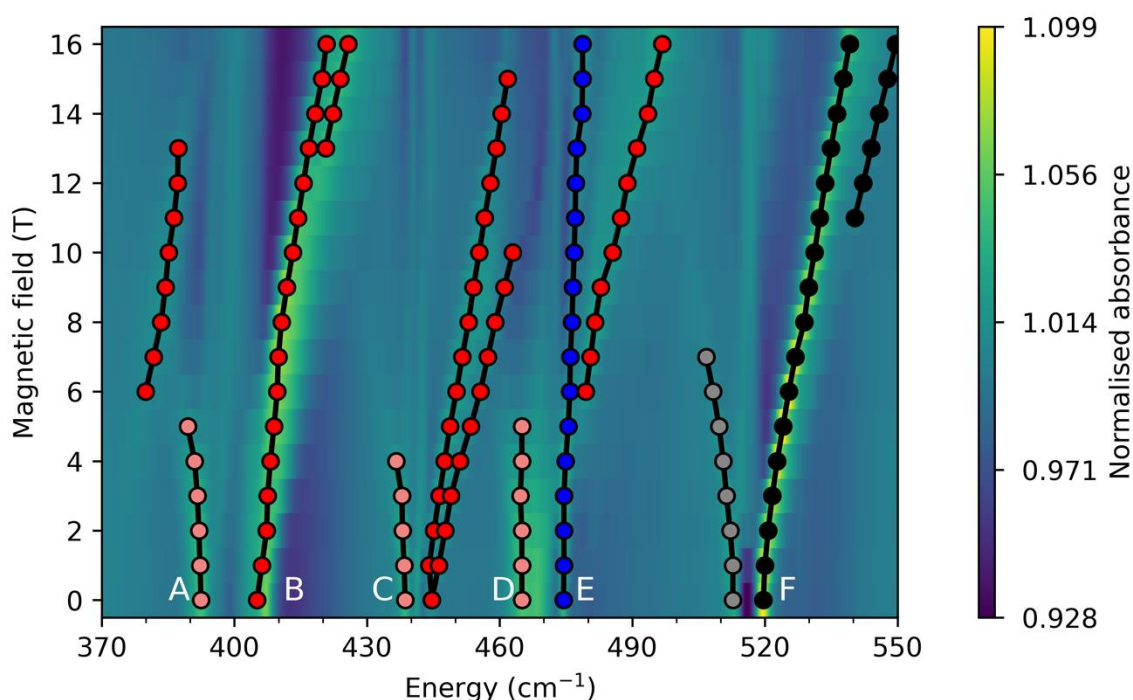


Figure 5. Experimental FIRMS map for 1 with transitions highlighted. Experimental FIRMS map in the range 370-550 cm^{-1} , with purely electronic transitions shown in blue, vibronic inter-KD transitions in black/grey (cold/hot), and vibronic intra-KD transitions in red/pink (cold/hot). Assignments are based on *ab initio* simulation (Figure 3c). Note that the weak field-independent signals (vertical lines) may be pure vibrational modes, but as they appear at the turning points of the raw transmission spectra they could very well be instrumental artefacts.

While the FIRMS map allows us to observe vibronic transitions, we have shown that such spectra are subject to an “envelope effect”, making them most sensitive to transitions near electronic excited states (Figure 4, Equations 3, S4 and S5). As such, these experiments do not provide a direct measure of the strength of the vibronic coupling for all modes. However, our high-quality modelling of the FIRMS map here serves as a detailed benchmark of our *ab initio* calculation of the vibronic coupling and, thus, we are in a position to examine the vibronic coupling strength of all vibrational modes. The values of S for all vibrational modes (Figures 6 and S14, Table S5) reveal that those in the 370-550 cm^{-1} region are not more strongly coupled than modes at other energies. While modes 35 and 36 (responsible for signal **B**) have the second-largest vibronic coupling overall, they have a similar value of S to modes 26 and 27 at 305 cm^{-1} , but we do not see any intra-KD transitions in this range in the FIRMS experiment; this is due to the envelope effect (Figure 4b). Overall, there are seven pairs of modes with $S > 1.5 \text{ cm}^{-1}$ (7, 8, 14, 15, 20, 21, 22, 23, 26, 27, 35, 36, 142 and 143); interestingly, these modes all have E-symmetry, which break the C_3 point symmetry of the equilibrium structure (see Supplementary Videos). However, it is not as simple as A- vs. E-symmetry dictating the strength of vibronic coupling: the modes listed above all involve significant distortions

to the first coordination sphere of Yb^{III} while, for instance, there are E-symmetry modes at 477 and 762 cm^{-1} (modes 41-42 and 58-59, respectively) that involve peripheral motion (see Supplementary Videos) and hence have small S values of 0.20 and 0.03 cm^{-1} , respectively. However, there are also A-symmetry modes that involve distortions to the first coordination sphere which have significantly weaker coupling than the modes that couple most strongly (e.g. mode 34 at 406 cm^{-1} with $S = 1.10 \text{ cm}^{-1}$). Therefore, we can conclude that modes that distort the first coordination sphere and also break the local point symmetry have the strongest vibronic coupling. Further corroborating this analysis, we find that there is excellent agreement between the strongly-coupled modes below 300 cm^{-1} and peaks 1a-d in the luminescence spectrum (Figures 2 and S15). Despite having very strong vibronic coupling, these features are weak in the FIRMS map due to the “envelope effect” (although can be observed, Figure S12), but appear in the luminescence spectrum as this is a spontaneous emission experiment compared to transitions driven by IR photons in FIRMS; the only outlier is the absence of modes 7 and 8 (99 cm^{-1} , $S = 2.03 \text{ cm}^{-1}$) in the luminescence spectrum which we cannot presently explain.

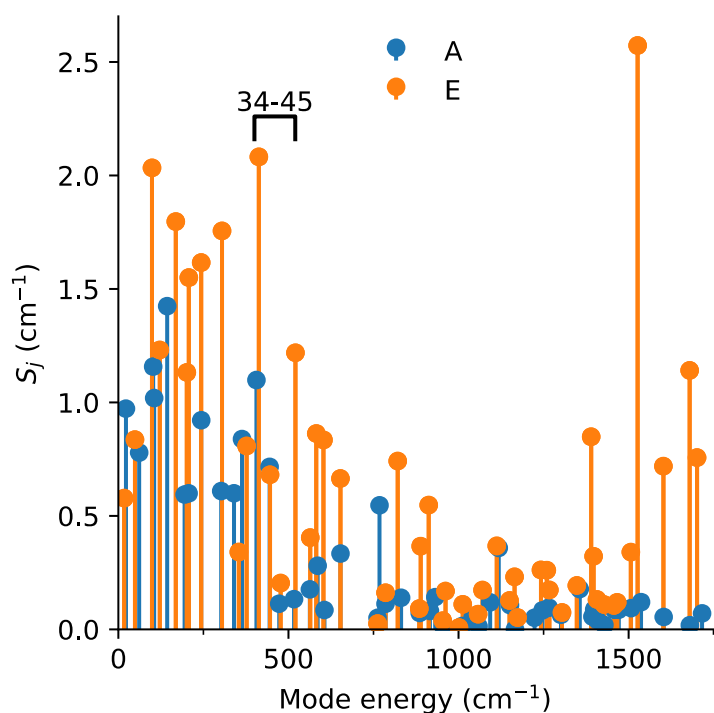


Figure 6. *Ab initio* calculated vibronic coupling strength. S_j of the vibrational modes of $\mathbf{1}_{\text{opt}}$ with A (blue) and E (orange) symmetry. Modes 34-45 are highlighted.

In summary, we have measured the FIRMS map for $[\text{Yb}(\text{trensal})]$ (**1**) and developed an *ab initio* model to calculate the vibronic coupling and hence simulate the map. Our theoretical model shows that vibronic transitions in FIRMS experiments are subject to an “envelope effect” and thus should be most intense near electronic excitations, explaining the structure of our spectra; this is a general

phenomenon that has not been found before. Our fully *ab initio* calculation of the FIRMS map shows excellent agreement with experiment and thus directly validates our approach for calculating vibronic coupling. Hence, we can determine the vibrational modes which are most strongly coupled to the electronic states; for [Yb(trensal)] these are E-symmetry modes involving significant motion in the first coordination sphere at 99, 169, 207, 243, 305, 413 and 1527 cm^{-1} . To extract yet more information on the vibronic coupling, future low energy (20-100 cm^{-1}) and single crystal FIRMS experiments will allow direct probing of acoustic phonon modes and anisotropy effects, respectively, which are both crucial in low-temperature Raman relaxation of SMMs and decoherence in spin qubits. Indeed, we can use the same computational methodology to predict magnetic relaxation due to vibronic coupling in single-molecule magnets,²⁸ and similar methods can be used to directly probe the contribution of vibronic coupling to decoherence in molecular qubits.²⁹ Only by combined experimental and theoretical studies such as these can we unravel the details of vibronic coupling in molecules and thus begin to develop guidelines for control of this crucial interaction.

Methods

FIRMS measurements

FIRMS measurements were made on 5 mg of a polycrystalline sample of **1** at 4.2 K for IR energies $<900 \text{ cm}^{-1}$ using a Bruker Vertex 80v vacuum FTIR spectrometer with a resolution of 0.3 cm^{-1} . FTIR spectra were recorded under a series of applied magnetic fields from 0 to 16 T in the Voigt geometry such that propagation of the incident radiation was perpendicular to the applied field. Transmission was detected using a Si bolometer placed immediately behind the sample (in the magnetic field) in order to minimize loss of power. Transmitted intensity spectra were measured in 1 T field steps. Here, the strong field-independent dips in transmission are due to a combination of electric-dipole-active vibrational absorptions and an instrumental function caused by standing waves in the far-IR propagation system (Figure S5a). To improve the signal-to-noise ratio, each FTIR measurement was repeated four times at each field step, then averaged. To distinguish field dependent excitations from those that are field independent, spectra at each magnetic field step were divided by the average of all spectra, resulting in clear “magnetic” spectral features above a more-or-less flat baseline and successful suppression of strong field-independent ‘dips’ in transmittance (Figure 3, Figure S5b). This normalisation procedure does, however, introduce artefacts wherever the raw transmission is near zero (e.g. around 0 and 720 cm^{-1} , Figure S5) due to division of zero-by-zero; these ‘blind spots’ are due to destructive interference in the beam splitter employed in the FTIR spectrometer. We note also that, outside of these blind spots, a few weak field independent signals remain after background division, which could also be instrumental artefacts as they occur at the turning points of the raw transmission spectra. As the measurements were performed on a polycrystalline sample, all

molecular orientations in the FIRMS map are sampled at once which, in turn, results in a continuous magnetic field dependent absorption profile superimposed onto the raw FTIR spectrum.

Ab initio calculations

Geometry optimisation and calculation of the normal modes of vibration of **1** was performed in the gas-phase using unrestricted DFT within the Gaussian 09 rev. D package.³⁰ The X-Ray crystallographic structure was used as a starting point, and all atomic positions were optimised simultaneously. The PBE0 density-functional was used in conjunction with Grimme's D3 dispersion correction,^{31–33} the cc-pVDZ basis set was used for carbon and hydrogen atoms and the cc-pVTZ basis set was used for nitrogen and oxygen atoms,^{34,35} while the Stuttgart RSC 1997 effective core potential (ECP) was employed for the 28 core electrons of ytterbium and the remaining valence electrons were described with the corresponding valence basis set.^{36–38} Symmetry was enabled in the optimisation to preserve the C₃ point group.

We use OpenMolcas to perform CASSCF-(XMS-CASPT2)-SO calculations for the crystallographic, optimised and distorted geometries of **1**.³⁹ Basis sets from the ANO-RCC library were employed with VTZP quality for Yb, VDZP quality for the N atoms and O atoms, and VDZ quality for all remaining atoms.^{40,41} Density fitting of the two-electron integrals using the acCD scheme was performed to speed up the calculations.⁴² The active space consisted of thirteen 4f electrons in the seven 4f orbitals of Yb^{III}. State-averaged CASSCF calculations were performed for seven roots of the S = 1/2 state and then mixed by spin orbit coupling using the RASSI module.⁴³ For the crystallographic and optimised structures, CASPT2 corrections to the energies of the seven S = 1/2 roots were calculated using the extended multistate (XMS) method prior to RASSI.⁴⁴ SINGLE_ANISO was used to decompose the spin orbit wave functions into the crystal field Hamiltonian formalism, using a fixed reference frame determined from the optimised structure.⁴⁵ Here we report the crystal field parameters in the context of the Stevens operator equivalent formalism (Table S8).⁴⁶

Data availability

Raw research data files supporting this publication are available at doi: xxxx

References

- 1 E. Collini, C. Y. Wong, K. E. Wilk, P. M. G. Curmi, P. Brumer and G. D. Scholes, *Nature*, 2010, **463**, 644–647.
- 2 H. Lee, Y.-C. Cheng and G. R. Fleming, *Science (80-.)*, 2007, **316**, 1462–1465.
- 3 J. C. Dean, T. Mirkovic, Z. S. D. Toa, D. G. Oblinsky and G. D. Scholes, *Chem*, 2016, **1**, 858–872.

- 4 A. Milo, E. N. Bess and M. S. Sigman, *Nature*, 2014, **507**, 210–214.
- 5 C. M. Marian, *Wiley Interdiscip. Rev. Comput. Mol. Sci.*, 2012, **2**, 187–203.
- 6 A. Gaita-Ariño, F. Luis, S. Hill and E. Coronado, *Nat. Chem.*, 2019, **11**, 301–309.
- 7 M. Shiddiq, D. Komijani, Y. Duan, A. Gaita-Ariño, E. Coronado and S. Hill, *Nature*, 2016, **531**, 348–351.
- 8 C. A. P. Goodwin, F. Ortu, D. Reta, N. F. Chilton and D. P. Mills, *Nature*, 2017, **548**, 439–442.
- 9 B. C. Paulus, S. L. Adelman, L. L. Jamula and J. K. McCusker, *Nature*, 2020, **582**, 214–218.
- 10 K. S. Pedersen, J. Dreiser, H. Weihe, R. Sibille, H. V. Johannesen, M. A. Sørensen, B. E. Nielsen, M. Sigrist, H. Mutka, S. Rols, J. Bendix and S. Piligkos, *Inorg. Chem.*, 2015, **54**, 7600–7606.
- 11 F. Liedy, J. Eng, R. McNab, R. Inglis, T. J. Penfold, E. K. Brechin and J. O. Johansson, *Nat. Chem.*, 2020, **12**, 452–458.
- 12 Y. Rechkemmer, F. D. Breitgoff, M. Van Der Meer, M. Atanasov, M. Haki, M. Orlita, P. Neugebauer, F. Neese, B. Sarkar and J. Van Slageren, *Nat. Commun.*, 2016, **7**, 10467.
- 13 D. H. Moseley, S. E. Stavretis, K. Thirunavukkuarasu, M. Ozerov, Y. Cheng, L. L. Daemen, J. Ludwig, Z. Lu, D. Smirnov, C. M. Brown, A. Pandey, A. J. Ramirez-Cuesta, A. C. Lamb, M. Atanasov, E. Bill, F. Neese and Z. L. Xue, *Nat. Commun.*, 2018, **9**, 2572.
- 14 D. H. Moseley, S. E. Stavretis, Z. Zhu, M. Guo, C. M. Brown, M. Ozerov, Y. Cheng, L. L. Daemen, R. Richardson, G. Knight, K. Thirunavukkuarasu, A. J. Ramirez-Cuesta, J. Tang and Z.-L. Xue, *Inorg. Chem.*, 2020, **59**, 5218–5230.
- 15 J. C. Hill and R. G. Wheeler, *Phys. Rev.*, 1966, **152**, 482–494.
- 16 A. J. Sievers and M. Tinkham, *Phys. Rev.*, 1963, **129**, 1995–2004.
- 17 B. M. Flanagan, P. V Bernhardt, E. R. Krausz, S. R. Lüthi and M. J. Riley, *Inorg. Chem.*, 2002, **41**, 5024–5033.
- 18 M. Perfetti, E. Lucaccini, L. Sorace, J. P. Costes and R. Sessoli, *Inorg. Chem.*, 2015, **54**, 3090–3092.
- 19 J. Dreiser, C. Wäckerlin, M. E. Ali, C. Piamonteze, F. Donati, A. Singha, K. S. Pedersen, S. Rusponi, J. Bendix, P. M. Oppeneer, T. A. Jung and H. Brune, *ACS Nano*, 2014, **8**, 4662–4671.
- 20 K. S. Pedersen, A. M. Ariciu, S. McAdams, H. Weihe, J. Bendix, F. Tuna and S. Piligkos, *J. Am. Chem. Soc.*, 2016, **138**, 5801–5804.

- 21 R. Hussain, G. Allodi, A. Chiesa, E. Garlatti, D. Mitcov, A. Konstantatos, K. S. Pedersen, R. De Renzi, S. Piligkos and S. Carretta, *J. Am. Chem. Soc.*, 2018, **140**, 9814–9818.
- 22 H. A. Kramers, *Proc. Acad. Sci.*, 1930, **32**, 1176.
- 23 J.-C. G. Bünzli and S. V. Eliseeva, in *Lanthanide Luminescence: Photophysical, Analytical and Biological Aspects*, eds. P. Hänninen and H. Härmä, Springer Berlin Heidelberg, Berlin, Heidelberg, 2010, pp. 1–45.
- 24 M. Atanasov and F. Neese, *J. Phys. Conf. Ser.*, 2018, **1148**, 012006.
- 25 R. Orbach, *Proc. R. Soc. London. Ser. A. Math. Phys. Sci.*, 1961, **264**, 458–484.
- 26 N. C. Chang, J. B. Gruber, R. P. Leavitt and C. A. Morrison, *J. Chem. Phys.*, 1982, **76**, 3877–3889.
- 27 J. Mulak and M. Mulak, *Phys. status solidi*, 2006, **243**, 2796–2810.
- 28 D. Reta, J. G. C. Kragsskow and N. F. Chilton, *ChemRxiv*, , DOI:10.26434/chemrxiv.13606556.v1.
- 29 L. Escalera-Moreno, N. Suaud, A. Gaita-Ariño and E. Coronado, *J. Phys. Chem. Lett.*, 2017, **8**, 1695–1700.
- 30 M. J. Frisch, G. W. Trucks, H. B. Schlegel, G. E. Scuseria, M. A. Robb, J. R. Cheeseman, G. Scalmani, V. Barone, G. A. Petersson, H. Nakatsuji, X. Li, M. Caricato, A. Marenich, J. Bloino, B. G. Janesko, R. Gomperts, B. Mennucci, H. P. Hratchian, J. V. Ortiz, A. F. Izmaylov, J. L. Sonnenberg, D. Williams-Young, F. Ding, F. Lipparini, F. Egidi, J. Goings, B. Peng, A. Petrone, T. Henderson, D. Ranasinghe, V. G. Zakrzewski, J. Gao, N. Rega, G. Zheng, W. Liang, M. Hada, M. Ehara, K. Toyota, R. Fukuda, J. Hasegawa, M. Ishida, T. Nakajima, Y. Hondo, O. Kitao, H. Nakai, T. Vreven, K. Throssell, J. A. Montgomery Jr., J. E. Peralta, F. Ogliaro, M. Bearpark, J. J. Heyd, E. Brothers, K. N. Kudin, V. N. Staroverov, T. Keith, R. Kobayashi, J. Normand, K. Raghavachari, A. Rendell, J. C. Burant, S. S. Iyengar, J. Tomasi, M. Cossi, J. M. Millam, M. Klene, C. Adamo, R. Cammi, J. W. Ochterski, R. L. Martin, K. Morokuma, O. Farakas, J. B. Foresman and D. J. Fox, *Gaussian 09, Revision D.01*, Wallingford CT, 2013.
- 31 S. Grimme, *J. Comput. Chem.*, 2006, **27**, 1787–1799.
- 32 S. Grimme, *J. Comput. Chem.*, 2004, **25**, 1463–1473.
- 33 J. P. Perdew, M. Ernzerhof and K. Burke, *J. Chem. Phys.*, 1996, **105**, 9982–9985.
- 34 D. E. Woon and T. H. Dunning, *J. Chem. Phys.*, 1993, **98**, 1358–1371.
- 35 T. H. Dunning, *J. Chem. Phys.*, 1989, **90**, 1007–1023.
- 36 A. Bergner, M. Dolg, W. Küchle, H. Stoll and H. Preuß, *Mol. Phys.*, 1993, **80**, 1431–1441.

- 37 M. Dolg, H. Stoll, H. Preuss and R. M. Pitzer, *J. Phys. Chem.*, 1993, **97**, 5852–5859.
- 38 M. Kaupp, P. v. R. Schleyer, H. Stoll and H. Preuss, *J. Chem. Phys.*, 1991, **94**, 1360–1366.
- 39 I. Fdez. Galván, M. Vacher, A. Alavi, C. Angeli, F. Aquilante, J. Autschbach, J. J. Bao, S. I. Bokarev, N. A. Bogdanov, R. K. Carlson, L. F. Chibotaru, J. Creutzberg, N. Dattani, M. G. Delcey, S. S. Dong, A. Dreuw, L. Freitag, L. M. Frutos, L. Gagliardi, F. Gendron, A. Giussani, L. González, G. Grell, M. Guo, C. E. Hoyer, M. Johansson, S. Keller, S. Knecht, G. Kovačević, E. Källman, G. Li Manni, M. Lundberg, Y. Ma, S. Mai, J. P. Malhado, P. Å. Malmqvist, P. Marquetand, S. A. Mewes, J. Norell, M. Olivucci, M. Oppel, Q. M. Phung, K. Pierloot, F. Plasser, M. Reiher, A. M. Sand, I. Schapiro, P. Sharma, C. J. Stein, L. K. Sørensen, D. G. Truhlar, M. Ugandi, L. Ungur, A. Valentini, S. Vancoillie, V. Veryazov, O. Weser, T. A. Wesolowski, P. O. Widmark, S. Wouters, A. Zech, J. P. Zobel and R. Lindh, *J. Chem. Theory Comput.*, 2019, **15**, 5925–5964.
- 40 B. O. Roos, V. Veryazov and P.-O. Widmark, *Theor. Chem. Acc.*, 2004, **111**, 345–351.
- 41 B. O. Roos, R. Lindh, P.-Å. Malmqvist, V. Veryazov and P.-O. Widmark, *J. Phys. Chem. A*, 2005, **109**, 6575–6579.
- 42 F. Aquilante, R. Lindh and T. Bondo Pedersen, *J. Chem. Phys.*, 2007, **127**, 114107.
- 43 P. Å. Malmqvist, B. O. Roos and B. Schimmelpfennig, *Chem. Phys. Lett.*, 2002, **357**, 230–240.
- 44 T. Shiozaki, W. Györfy, P. Celani and H.-J. Werner, *J. Chem. Phys.*, 2011, **135**, 081106.
- 45 L. Ungur and L. F. Chibotaru, *Chem. - A Eur. J.*, 2017, **23**, 3708–3718.
- 46 K. W. H. Stevens, *Proc. Phys. Soc. London Sect. A*, 1952, **65**, 209–215.

Acknowledgements

We thank The University of Manchester for access to the Computational Shared Facility, the EPSRC (studentship to J.G.C.K.), and The Royal Society (University Research Fellowship to N.F.C.). This project has received funding from the European Research Council (ERC) under the European Union's Horizon 2020 research and innovation programme (grant agreement No. 851504) and the US National Science Foundation (NSF grant numbers DMR-1610226 and DMR-2004732). A portion of this work was performed at the NHMFL which is supported by the NSF (grant number DMR-1644779) and the State of Florida. S.P. thanks the VILLUM FONDEN for research grant 13376. We thank Prof. Richard Winpenny, Prof. Eric McInnes and Dr David Mills for insightful comments.

Author contributions

J.M. and S.H. designed the experiment. C.D.B. synthesised and purified the compound. S.P performed and interpreted the luminescence experiments. J.M., J.N. and M.O. performed the FIRMS measurements. J.G.C.K. and N.F.C. developed theory, wrote code, performed calculations and interpreted spectra. J.M., J.G.C.K., S.H. and N.F.C. wrote the manuscript with contributions from all authors.

Additional information

Supplementary information is available in the online version of the paper. Correspondence and requests for materials should be directed to S.P., S.H and N.F.C.

Competing financial interests

The authors declare no competing financial interests.